BioDOME: Concept of an EDL System for Returning Small Biological Samples from LEO

Grant Rossman[(1)], **Matthew LeVine**[(1)], **Sean Lawlor**[(1)], **Tyler Sloss**[(1)], **Pranay Mishra**[(1)], **Zu Puayen Tan**[(1)] **and**

Robert D. Braun[*(1)]

[(1)]*Georgia Institute of Technology, North Avenue, Atlanta, GA 30332*

ABSTRACT

A conceptual design of an Earth return vehicle is presented with the goal of safely returning biological samples from orbit. Key entry, descent, and landing trade studies were completed at the conceptual level for two different mission scenarios: return from the International Space Station (ISS) and an autonomous, free-flying vehicle returning from Low Earth Orbit (LEO). The analyses that follow for each key subsystem drove design decisions to create the **Bio**pan **D**eployment in **O**rbit for **M**icrogravity **E**xposure (BioDOME) vehicle with the versatility to satisfy both of the aforementioned mission scenarios.

The final design features a ballistic entry, a $45°$ spherecone aeroshell with a diameter of 88-cm, a PICA heatshield with a thickness of 7.7 cm, and a passive landing system containing an 8-m diameter ringsail parachute combined with a 7.8-cm thick crushable carbon foam. Analysis of the vehicle performance verified survivability of biological samples due to heat and deceleration loads from entry. Trajectory dispersion analysis yielded crossrange and downrange limited to ±1.5-km and ±30-km, respectively, while landing velocity was confirmed to be ≤ 4.0-m/s for all cases.

1. PROBLEM STATEMENT & REVIEW OF EXISTING CONCEPTS

Since the retirement of the space shuttle, the International Space Station (ISS) is currently the primary orbital platform for performing experiments with biological samples. Transportation of samples to and from the ISS are accomplished by the Russian Soyuz and Progress spacecraft [1], the Japanese Kounotori vehicle (HTV) [2], the European Automatic Transfer Vehicle (ATV) [3], and the USA's Dragon [4] and Cygnus [5] spacecraft. However, transportation via these existing spacecraft are expensive and non-frequent, which does not meet the requirements of small-budget agencies conducting time-sensitive biological experiments. The goal of this study is to design a conceptual small reentry system for the recovery of biological samples flown in Low Earth Orbit, including options for both ISS interface as well as

a free-flyer concept.

At the beginning of the design process, a few past and current Earth reentry vehicles were reviewed. The first vehicle surveyed was the Stardust reentry capsule, which was designed to capture and return samples from the freestream emanating from the tail of the comet Wild-2 [6]. The Stardust capsule, as demonstrated by the cross-sectional diagram in Fig. 1, is approximately 0.8-m in diameter with a mass of 45.8-kg. The windward side is a blunted $60°$ (half-angle) sphere-cone, while the leeward side is a truncated cone. Although the capsule was not designed for biological samples, there are two design characteristics relevant to this design problem: 1) a clamshell design that opens in flight to expose the sample tray to space, and 2) a passive, ballistic flight-path that landed successfully within the Utah Test and Training Range (UTTR).
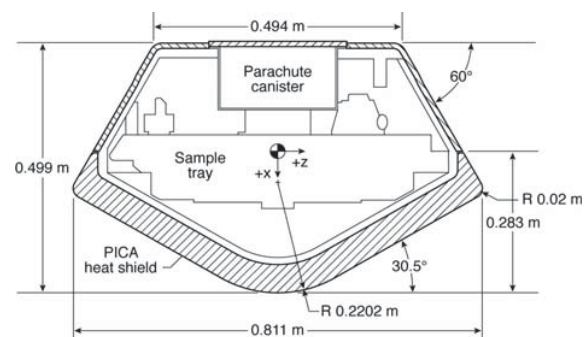

Fig. 1. Stardust Capsule Configuration [6]

The next few concepts surveyed were vehicles currently under development to accomplish sample return from the ISS. An example of a cutting-edge, small reentry vehicle is the RED-4U by Terminal Velocity Aerospace (TVA) [7]. TVA developed a series of small EDL vehicles under the "RED" family name, including the operational 36-cm diameter, 28-cm high and 8.6-kg RED-Data, which is used purely to study reentry and break-up physics [8]. On the other hand, the future slightly larger RED-4U will be sized to return small payloads with an equivalent payload volume to a 4U CubeSat, which could potentially include biological samples. The

---

[*]David and Andrew Lewis Professor of Space Technology, Guggenheim School of Aerospace Engineering

RED vehicles are $45°$ (half-angle) sphere-cones, similar to NASA's Mars Microprobe design. The geometry is optimized to provide stable and predictable orientation during reentry. These two qualities are highly desirable for small EDL vehicles to allow for passive reentry and minimal trajectory guidance input.
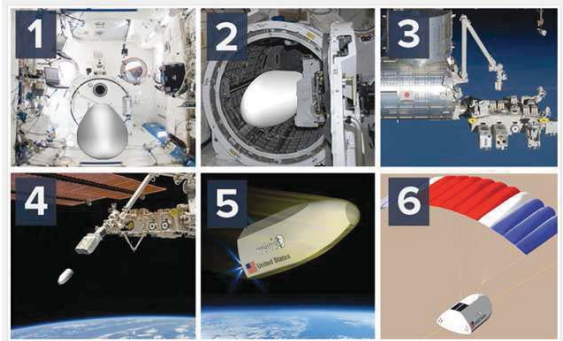

Fig. 2. Schematic of TRV's Concept of Operations [9]

Another biological sample-return vehicle is the Terrestrial Return Vehicle (TRV), whose concept of operations is depicted in Fig. 2 [9]. TRV is an unconventional lifting-entry vehicle that can be brought inside the ISS through the cargo airlock. This is a unique design capability that allows astronauts to work on the payload of TRV without the limitations and dangers of space-walks. However, this limits the TRV's diameter to the airlock hatch diameter. For reentry, the TRV is launched directly from the Japanese Experiment Module Robotic Manipulator System (JEMRMS). After successful detachment from the ISS using JEM, the TRV must perform a de-orbit burn, a controlled hypersonic deceleration, and a descent under directionally controlled parafoil. While this design represents a unique solution, the aerodynamic design is very complex. in addition, there are many safety concerns associated with bringing a vehicle inside the ISS with an exposed propulsion system.

Fig. 3. Biopan Before (left) and After (right) Flight

The final system surveyed was the European Space Agency's Biopan facility, which is affixed to a Russian Foton capsule and flown on a near-circular orbit at a $62°$ inclination angle for 10-14 days. Biopan

is a closed biological sample system, resembling a circular clamshell design, that can carry 5-kg of payload. Experimental samples can have a maximum height of 25-mm and and a maximum total mounting area of 1080-cm^2, as shown in Fig. 3. During orbit, Biopan's lid can be opened $180°$, exposing the experiments to space. This capability is particularly suitable for studying the robustness of life in hostile extraterrestrial environments [10]. When closed, Biopan's internal temperature can be maintained between $5 - 25\,°C$ throughout orbit and reentry. If an uncontrolled thermal environment is desired, temperatures may fluctuate between -35 and $35\,°C$. Before reentry, Foton's reentry modules separates from the service module and the battery. Biopan is mounted on the spherical reentry module, protruding from the thermal blanket as demonstrated in Fig. 4, and thus requires a significant ablative heatshield for thermal protection. Biopan is a well-tested system, and the Foton architecture is a good example of a free-flyer mission. Foton, however, is a large vehicle that carries many microgravity experiments inside the spherical reentry module, and it is not designed to interface with the ISS.
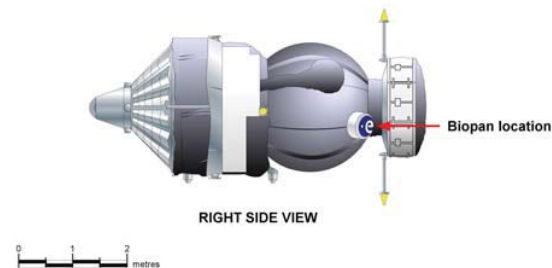

Fig. 4. Foton Capsule with Biopan Location

2. MISSION CONCEPT & CONSTRAINTS

After reviewing the existing vehicles above, the problem was recast as designing a reentry vehicle specifically for the Biopan facility as an alternative to mounting on a Foton vehicle. The Biopan design can be used as a flight-proven, biological sample enclosure system for this mission without significant modifications. The new design, heretofore referred to as the **Bio**pan **D**eployment in **O**rbit for **M**icrogravity **E**xposure or **BioDOME**, will mimic the Foton architecture for the free-flyer concept, relying on an attached battery and service module in orbit and separating before reentry. BioDOME, however, shall be significantly smaller in mass and volume, more closely approaching the dimensions of a vehicle like Stardust. Additionally, this smaller system shall have a capability of interfacing with the ISS to return long-term experiments from the EXPOSE facility.

When considering a biological sample return from the ISS, the first consideration is how astronauts may need to interact with the samples/reentry vehicle. Investigations and analysis will determine if the entire BioDOME reentry vehicle must enter the ISS, or just the Biopan sample enclosure. The first assumption made is that BioDOME will not be large enough to attach with the human airlocks on the ISS. The two areas where the vehicle would station itself is either near the *Exposed Facility* (JEM-EF) port or through one of the smaller cargo hatches such as on the Japanese Experiment Module *Kibo*. This module has the advantage of a 10-m long remote manipulator system which could "catch" BioDOME to bring inside the ISS. Alternatively, the remote manipulator can be used to remove Biopan from the vehicle while it is docked at the JEM-EF and bring Biopan inside [11]. The vehicle entering the ISS has constraints because the Kibo module has a fixed diameter of 60-cm. After including a 10-cm margin for hatch clearance, BioDOME could be no wider than 50-cm in diameter. Reentry vehicles with smaller diameters cannot easily reduce ballistic coefficient, which has an adverse effect on $C_D A$. Additionally BioDOME would be carrying propellant aboard for its RCS system, but normal ISS protocol would not allow the vehicle within the human rated modules. If only Biopan is to enter the ISS, the first technical consideration is how Biopan would be extracted from BioDOME and brought inside. Most spacewalks completed by astronauts aboard ISS are designed and practiced well before they even reach the station. If a spacewalk is required to extract Biopan from BioDOME it would require additional planning by ISS mission control to accommodate the payload [12]. If instead the manipulator arm is used, the Biopan must be separated from BioDOME and placed within the cargo hatch where it is easily retrievable. In this scenario, the $C_D A$ of the reentry vehicle can be increased, effectively lowering the overall ballistic coefficient which in turn can mitigate some of the aerothermal conditions BioDOME will experience during reentry.

Given that it was designed to fit on the outside of the Foton reentry capsule, Biopan was typically exposed to significant linear decelerations and heating conditions. The maximum linear decelerations experienced by payloads on Foton missions are ±16g for a period of no longer than 20-seconds and ±9g for a period of no longer than 100-seconds [13]. While small biological samples such as bacteria have been shown to survive and grow under hyper-accelerations exceeding 400,000g [14], the maximum decelerations for BioDOME shall be conservatively constrained to match or reduce those experienced by the Biopan while attached to a Foton capsule. The maximum convective heat-rate and wall temperatures experienced by the Foton capsule are 1600 kW/m^2 (160 W/cm^2) and 2000 °C, respectively.

These heating conditions are much more constraining for biological sample accommodation, and as a result Biopan was over-fitted with a quite massive heatshield, as diagrammed in Fig. 5. The entire Biopan system had a budgeted mass of 27-kg with 12-kg allotted to this significant heatshield to prevent temperatures inside Biopan from exceeding $+30$ °C [15].
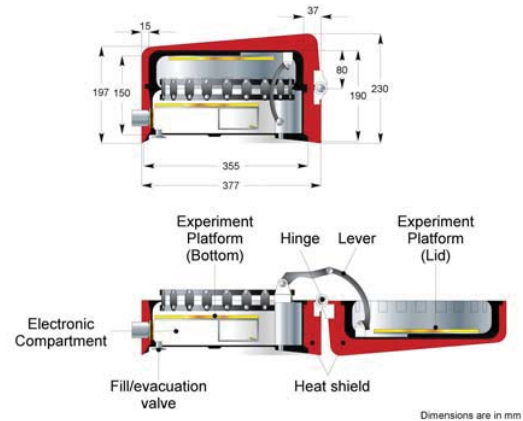

Fig. 5. Biopan Cross-Section and Dimensions

For the current concept, the reentry system shall accommodate the Biopan within its aeroshell, and thus the 12-kg heatshield will not be necessary for the Biopan (although an equivalent shield shall be required for the full BioDOME system). The rest of the Biopan design shall remain unchanged, with 10-kg allotted for structure and instrumentation (including temperature control and hermetic seal capabilities), and 5-kg allotted for biological payload. The minimum diameter of BioDOME shall be set by the dimensions of Biopan (sans heatshield) from Fig. 5, with the maximum diameter being constrained to 97-cm as dictated by the payload fairing of a Pegasus® launch vehicle [16]. If the entire vehicle is intended to be brought inside the ISS, the maximum diameter constraint must be reduced to 57.6-cm as dictated by the airlock on the Japanese Experimental Module *Kibo* [11].

3. AEROSHELL DESIGN & AEROTHERMODYNAMICS

Due to the small size of the return payload and the dense atmosphere of Earth, literature studies recommend the use of a sphere-cone aeroshell design. A modified Newtonian [17] sphere-cone panel code was developed and executed to analyze and perform various trade studies on the design of the entry vehicle aeroshell. This code was linked to planar equations of motion for analyzing the trajectory of the given return vehicle for suitability with the use of biological samples given the latter constraints. The analysis also incorporated

a first order numerical analysis [18] of the heat shield using phenolic impregnated carbon ablator (PICA) [19] material in order to size the heat shield for each analyzed sphere-cone configuration. PICA was chosen as the ablative material because of its relatively low density of 265 kg/m^3. While SLA-561V [20] has a comparable density, PICA can handle much higher peak heat rates which allows greater flexibility for balancing trajectory design and aerothermodynamic constraints.
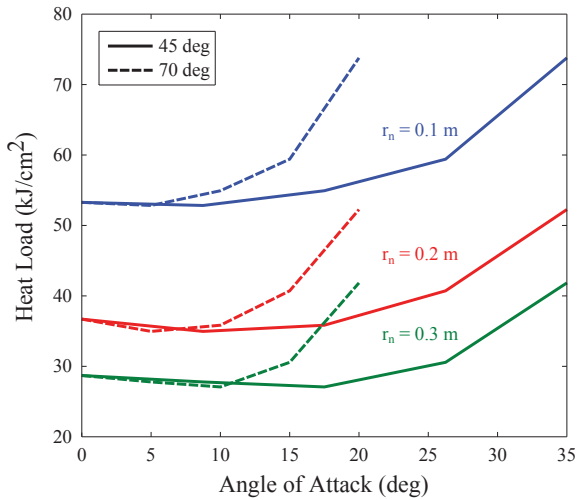

Fig. 6. Integrated Heat Loads for Lifting Vehicles

One of the first trade studies analyzed the potential benefit for using a lifting versus a ballistic entry. This lifting study investigated several sphere-cone configurations and showed that for a given constant peak deceleration, the integrated heat load benefited from a certain small angle of attack. However, this benefit was small and it was decided that the added complexity of designing the system for lifting entry outweighed the heat-load savings, and all design considerations moving forward were limited to ballistic entry concepts. The results of this study for various sphere-cone half angles and nose radii are shown in Fig. 6. A reduction in heat load was seen for small angles of attack, but at larger angles of attack the integrated heat load increased significantly. This was attributable to the behavior of the drag coefficient. As the angle of attack increased above $\sim 5-10$ degrees, the drag coefficient for the sphere cone began to significantly decrease. The resulting increase in ballistic coefficient implied a longer vehicle flight time for a given flight path angle, and thus a larger integrated heat load.

The next studies performed on the aeroshell design investigated the overall size of the vehicle. Fig. 7 shows three $45°$ sphere-cone configurations with differing maximum diameters of 0.6-m, 0.8-m and 1.0-m, respectively. These plots show the heatshield required

thicknesses based on a maximum bondline temperature of $250\,°C$. As can be seen, the smallest diameter selected required a heatshield that was disproportionately large for the vehicle, leaving too little packing room for payload and other necessities for the entry vehicle. The design also pushed the center of pressure forward into the heatshield, implying that the stability of the vehicle would be compromised.
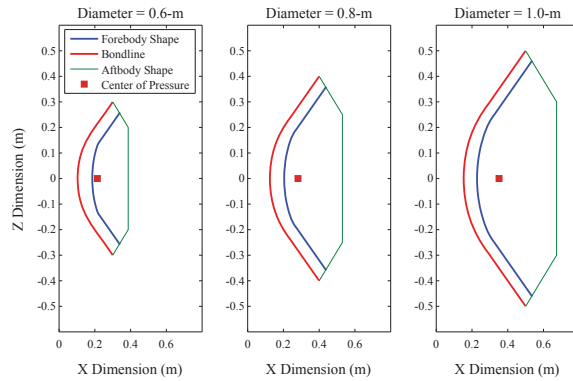

Fig. 7. Entry Vehicle Sizing Trade Study

This analysis essentially eliminated the concept of bringing the entire vehicle inside the ISS, as it becomes too constraining on the aerothermodynamic design of the vehicle. While it was understood that the 1.0-m diameter vehicle would be too large for the chosen launch vehicle's payload fairing, it was included in the analysis to assess the possible benefits of choosing a larger diameter and a larger launch vehicle. However, the largest vehicle was more massive and did not demonstrate a strong benefit over the medium sized vehicle. Thus, the 0.8-m design was targeted, allowing a little room for vehicle diameter creep while staying within the confines of the Pegasus® launch vehicle.
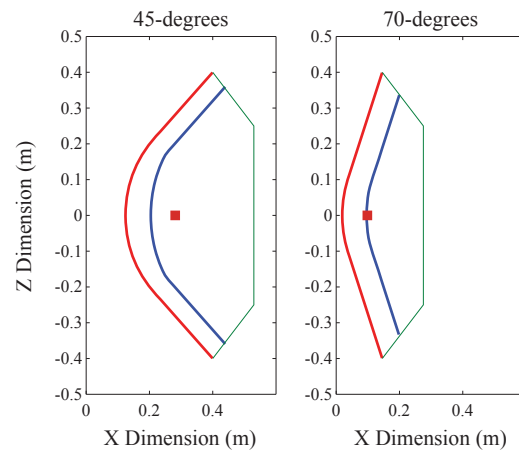

Fig. 8. Geometry for Sphere-Cone Angle Trade Study

Given the approximate vehicle size, the next studies investigated other aeroshell and trajectory design parameters including nose radius, entry flight path angle, and cone half-angle. Two cone angles of $45°$ and $70°$ were examined for several nose radii. Fig. 8 shows a plot of the aeroshell shapes for the $45°$ and $70°$ sphere-cones, while Table 1 shows a comparison of the performance characteristics. The $70°$ sphere-cone shows a lower calculated bondline temperature for the same entry flight path angle, but the vehicle has very low stability as shown by the extreme forward location of the vehicle center of pressure.

Table 1. Performance Characteristics for Sphere-Cone Angle Trade Study

| Metric	45 degree	70 degree
Angle of attack [deg]	0	0
C_L	0	0
C_D	1.052	1.631
L/D	0	0
Beta [kg/m^2]	142.8	70.5
Flight Time [sec]	685.1	729.5
Peak Decel [Earth g]	15.5	15.9
Peak Heat Rate [W/cm^2]	231.1	171.8
Heat Load [J/cm^2]	11722.5	8581.0
Downrange [km]	995.1	2357.7
Initial Flight Path Angle [deg]	5.0	5.5
Cone Half Angle [deg]	45	70
Cone Base Radius [m]	0.4	0.4
Effective Nose Radius [m]	0.3	0.3
Center of Pressure [m]	0.281	0.099
$T_{w,max}$ [K]	2594.3	2408.9
Ablation [cm]	0.466	0.301
Bondline Temp [K]	505.2	504.0
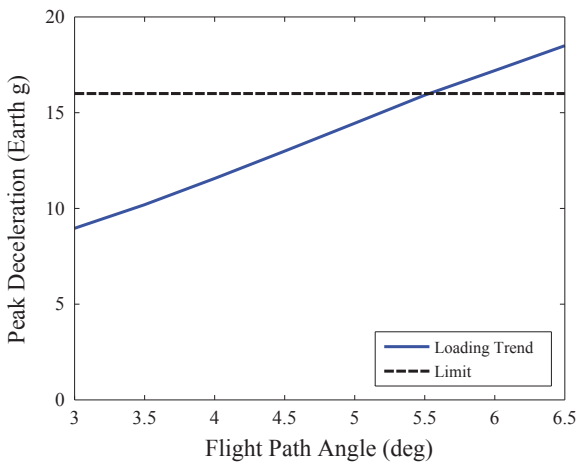
Fig. 9. Peak Deceleration vs Flight-Path Angle Trade Study

For both of these configurations various nose radii and flight path angles were investigated. Due to the similar ballistic coefficients of both vehicles, the peak deceleration followed the same trend for all configurations examined versus flight path angle. Fig.

9 shows that peak deceleration increases as flight path angle increases up to our assumed allowable peak deceleraon of 16g's at a flight path angle of $5.5°$, setting the upper limit on the flight path angle corridor. The lower limit was determined to be at approximately $0.5°$ flight-path angle, as shallower entry angles tended to lead to altitude climbing and sometimes atmosphere skip-outs regardless of ballistic coefficient, as demonstrated in Fig. 10. Thus, the flight corridor is defined on the range $[0.5°, 5.5°]$.
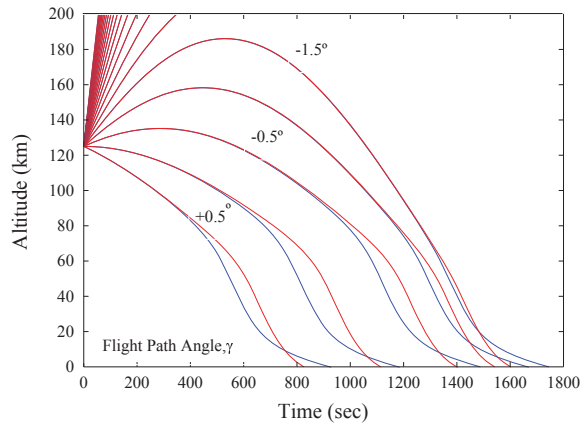

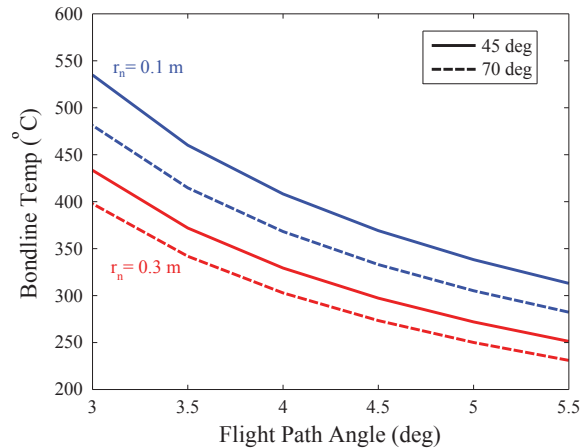Fig. 10. Minimum Flight-Path Angle and Atmosphere Skip-Out

Fig. 11. Bondline Temperature vs Flight-Path Angle Trade Study

The nose radius was selected by investigating the trends of bondline temperature and ablation levels for various configurations. These analyses are shown in Figs. 11 and 12. This analysis shows the trends that increasing nose radius had a large effect on reducing heat shield bondline temperature and ablation, which reduces the overall required thickness. This demonstrates a need to choose

the largest reasonable nose radius of 0.3-m. The analysis also shows the tradeoff between peak deceleration and required heatshield thickness for increasing flight-path angle. The maximum flight-path angle is constrained by the maximum allowable peak deceleration, but reducing the flight path angle significantly increased the bondline temperature and ablation depth. Thus, a nominal flight-path angle of $5.5\,^\circ$ was targeted for the final trajectory.
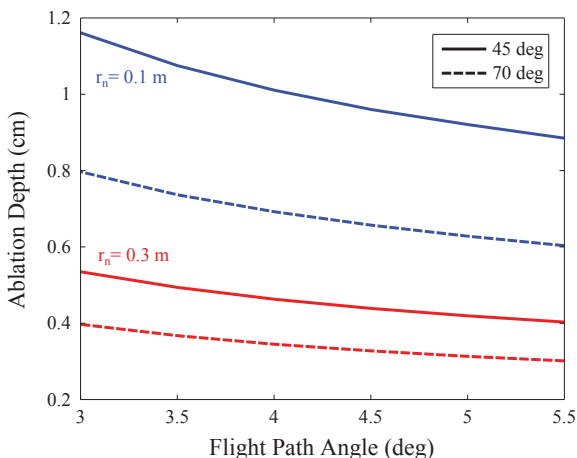

Fig. 12. Bondline Ablation Depth vs Flight-Path Angle Trade Study
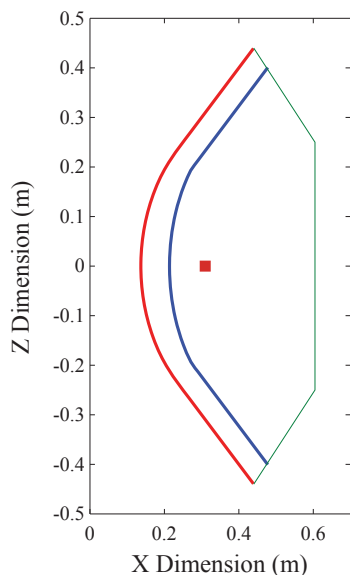

Fig. 13. Final Reentry Vehicle Geometry

Once the final aeroshell sizing was completed, the final configuration for BioDOME could be analyzed. As other flight and landing systems were designed and the mass budget of the reentry vehicle was updated, the

ballistic coefficient gradually increased from the earlier trade studies. As a result, the maximum allowable flight path angle was updated to be $5\,^\circ$ to keep peak deceleration below 16g's. The final vehicle diameter was also increased slightly to 88-cm for volumetric accommodation of landing systems. This resulted in the following design for BioDOME with a 7.7-cm thick heatshield as shown in Fig. 13. The performance characteristics for this final design are listed in Table 2.

Table 2. Final Reentry Vehicle Performance Characteristics

Metric	Final Design
Angle of attack [deg]	0
C_L	0
C_D	1.052
L/D	0
Beta [kg/m^2]	116.0
Flight Time [sec]	1289.1
Peak Decel [Earth g]	15.4
Peak Heat Rate [W/cm^2]	198.2
Heat Load [J/cm^2]	10056.2
Downrange [km]	978.3
Initial Flight Path Angle [deg]	5.0
Cone Half Angle [deg]	45
Cone Base Radius [m]	0.44
Effective Nose Radius [m]	0.33
Center of Pressure [m]	0.310
$T_{w,max}$ [K]	2496.5
Ablation [cm]	0.384
Bondline Temp [K]	510.7

4. PARACHUTE & LANDING SYSTEMS

To determine the final landing velocity of the BioDOME vehicle, iterative sizing calculations were performed for the parachute system and the landing system. A series of trade studies investigated a parachute/landing system combination that yielded the least mass while fitting within the volume of the final vehicle (see Fig. 13). A ringsail parachute was chosen after an extensive literature search due to its combination of good stability, superior performance at subsonic speeds, low mass, and low deployment risk. A hemispherical crushable landing system complements the parachute system allowing for energy absorption during a passive landing at UTTR. This static, crushable system was chosen for its negligible deployment risk and low mass when compared with an airbag landing system. The hemispherical crushable system also provided payload protection for the widest range of anticipated landing angles, which eliminated the need for a landing orientation control system.

The final landing velocity was the major factor driving the design of both the parachute and crushable system. After a few sizing iterations, it became apparent that the parachute and crushable system were competing factors. As shown in Figs. 14 and 16, lowering landing velocity decreased the crushable system's mass, but required a

larger parachute mass, and vice versa. The goal of the analysis was to achieve the lowest combined parachute and landing system mass while making sure that the internal volume constraint was not violated.

Initial analysis of the BioDOME vehicle indicated that the combined parachute-crushable system mass to satisfy landing constraints was prohibitively large. As such, a modified two-event deployment scheme was implemented to reduce the minimum parachute size. In this scheme, the parachute deploys at a higher altitude to slow the vehicle to a target velocity. Upon approaching the landing altitude, the primary structure of the vehicle (i. e. heat-shield, RCS, and avionics) will be ejected, leaving only the BioPAN and crushable landing system attached to the parachute. This allows the parachute to land a smaller mass, resulting in a significantly reduced parachute size. The trade studies shown in Figs. 14 and 16 assume this modified landing scheme. The following sections delve into detail about each trade study, justifying the finalized landing system sizing decisions.

4.1 Parachute Sizing & Mass Estimation

Given the dense Earth atmosphere and the small size of the reentry vehicle, BioDOME only requires parachute deployment at subsonic terminal velocities, which occurs at roughly 3000-m above the landing site. Since BioDOME will not be carrying humans or animals as payload, a singular subsonic parachute is preferred. A ringsail type parachute was selected for its high drag coefficient of around 0.8 (the highest among flight-tested parachutes), good-to-moderate stability, relatively light weight, and an extensive flight heritage for earth-reentry systems [21].

The parachute diameter was sized using a simple force-balance equation for the intended touchdown velocity of around V_{land} = 4-m/s, which was chosen to yield acceptable crushable landing support stroke-length and impact deceleration (see Section 4.2). It is assumed that BioDOME's drag is negligible compared to the parachute's drag. Therefore:

$$D_{chute} = 2\sqrt{\frac{1}{\pi}\left(\frac{2m_{vehicle}g_0}{\rho_0 V_{land}^2 C_D}\right)} \qquad (1)$$

The mass of the parachute was calculated assuming MIL-C-7020 Type II (T2) ripstop nylon [22] as the material of choice, with a density of ≤ 54.25 g/m^3. This nylon is a heavier and sturdier version of the nylon used on Mars Exploration Rover [23]. Thus:

$$m_{chute} = \rho_{material} A_{chute} \qquad (2)$$

The length of the suspension lines and bridles are estimated using Eqn. (3):

$$l_{lines} = \sqrt{\frac{D_{chute}^2}{2} + 100 D_{vehicle}^2} \qquad (3)$$

And the equivalent total cross-sectional area of the Kevlar lines is defined in Eqn. (4), where the denominator is found to be a typical rated stress load of Kevlar lines on parachute systems. Then:

$$A_{lines} = \frac{m_{vehicle}g_0 n_{max}}{675.8 \times 10^6 \text{ Pa}} \qquad (4)$$

$$m_{lines} = \rho_{Kevlar} A_{lines} l_{lines} \qquad (5)$$

The mass of the bridle + parachute suspension lines was sized assuming 10 vehicle diameters between the canopy and BioDOME, but this accounted for a negligible portion of the parachute's mass. The mortar and sabot system was sized using the formulations defined by Pleasants [24]. Finally, the volume of the packed system was sized as follows in Equation (6) assuming a packed density of 0.64 g/cm^3, which was in line with a hydraulic/vacuum-packed system [25].

$$V_{total} = \frac{m_{chute} + m_{lines}}{0.64 \text{ g/cm}^3} \qquad (6)$$

These equations were used to construct a curve that defined the mass and diameter of the parachute for a given desired landing velocity, as is displayed in Fig. 14. From these calculations, the final parachute system has a canopy diameter of 8-m, a system volume approximately corresponding to a 20-cm sided cube, and a total system mass of around 13.2-kg to enable the specified touchdown velocity.
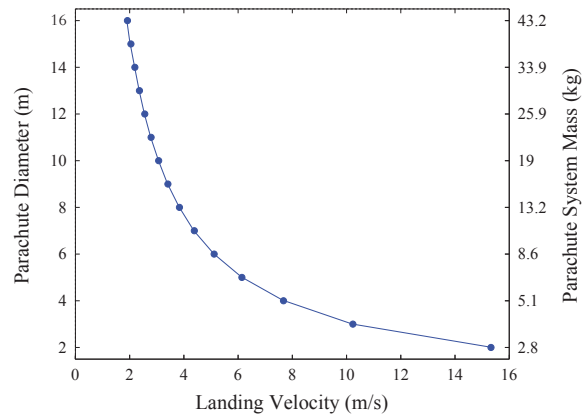

Fig. 14. Parachute Mass and Diameter vs Desired Landing Velocity

4.2 Sizing for Crushable Landing System

An iterative sizing procedure was performed to find the optimal landing velocity required to produce a parachute/landing system of the minimum mass able to fit within the allotted internal vehicle volume. Design requirements for the BioDOME crushable landing system include: 1) the vehicle must slow from landing velocity to a negligible velocity, 2) the system must be passive, and 3) the vehicle must be able to sustain impact for any feasible angle relative to the ground. Using a crushable system for impact deceleration is advantageous in many ways. Traditionally, crushables have low complexity, no deployment risk, and low mass when compared with other deceleration solutions. Airbags were also considered as a deceleration mechanism. The increased mass, volume, and complexity that resulted from airbag integration showed that this system is infeasible for this small vehicle.

A first-order technique was used for the conceptual design of the crushable landing system to keep the acceleration at impact below 16g [26]. This technique assumed conservation of kinetic and potential energy of the landed mass at touchdown. After incorporating the material properties of the foam, the crushable system was seen to perform work on the landed mass to bring its combined kinetic and potential energy to zero.

Equation (7) below shows the final stroke length, s_f, as a ratio of kinetic energy to desired maximum acceleration at impact, n_{max}.

$$s_f = \frac{V_i^2}{2g\left(n_{max}\eta - 1\right)} \qquad (7)$$

Equation (8) incorporates this final stroke length, s_f, with a pre-defined material strain, ϵ_f, to obtain a required initial height of the crushable system, s_0.

$$s_0 = \frac{s_f}{\epsilon_f} \qquad (8)$$

Equations (9) through (11) below show how to calculate a few more crucial parameters related to sizing the crushable system. These parameters are the required contact surface area for a uniform crushable ($A_{required}$), maximum stress (σ_{max}), and maximum impact acceleration felt by the vehicle in Earth g's (n_{max}).

$$A_{required} = \frac{n_{max}mg}{\sigma_{max}} \qquad (9)$$

$$\sigma_{max} = \frac{F_{max}}{A_{required}} \qquad (10)$$

$$n_{max} = \frac{F_{max}}{mg} \qquad (11)$$

Cylindrical crushable systems composed of both polyurethane foam and carbon foam were considered in the initial design [26]. Both systems have flight heritage on previous missions, serving as strong candidates for BioDOME. For a target landing velocity of approximately 5-m/s, cylinder heights of 21-cm and 15-cm for polyurethane foam and crushable foam, respectively, were determined to be too thick to fit in the vehicle. After realizing an alternative geometry would be required for the crushable design, literature reviews revealed that a hemispherical crushable concept may be a feasible option. A sizeable research effort was completed around the early 2000's by Mitcheltree, Braun, and Kellas to develop a suitable crushable system able to withstand an impact velocity of approximately 40-m/s from a passive entry vehicle for a Mars Sample Return mission [27, 28, 29]. Kellas completed a successful series of droptests with the revolutionary hemispherical crushable design diagrammed in Fig. 15.
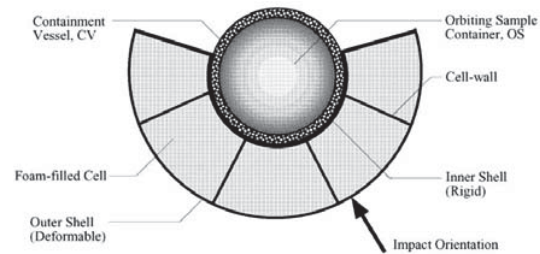

Fig. 15. Kellas' Hemispherical Crushable Concept

Kellas' crushable system offers many advantages for a passive landing. The honeycomb "soccer ball" structure provides extra strength to the system, while the hemispherical shape is able to withstand a variety of passive impact angles. Additionally, the crushable hemisphere is designed to withstand impact from rocks at UTTR, which is the chosen landing site for BioDOME. Using Kellas' stress-strain curves for polyurethane foam and carbon foam, the hemispheres were sized in an ultra-conservative fashion. The initial crushable thickness was sized using the same energy method described previously and used as the hemisphere shell thickness around the entire Biopan system. A carbon foam hemisphere shows considerable savings on thickness, only requiring a shell 7.8-cm thick to withstand an nmax of 16g's at a landing velocity of 4-m/s. Another quantity that must be determined is the landing velocity. A smaller landing velocity requires a thinner crushable with a larger parachute, and vice versa.

As can be seen, the carbon foam option allows for a much thinner crushable system by a large margin. Fig. 16 shows the total passive landing system mass (required parachute mass plus required crushable mass) and required hemisphere thickness as a function of landing velocity for both polyurethane and carbon foam. After considering the volume and mass constraints of the vehicle, a hemispherical, carbon foam crushable system was selected with a shell-thickness of 7.8-cm and a final landing velocity of 4-m/s. In this case, the combined mass of the crushable system and the parachute was only 15.2-kg, which provides a balance between key trades.
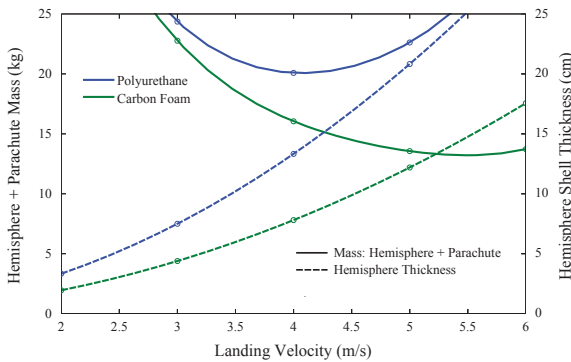

Fig. 16. Crushable Mass and Thickness versus Landing Velocity

The area required to support the crushable system is approximately 41.39-cm^2 as calculated by Eqn. (9). During impact, Biopan will be encapsulated by the hemispherical foam crushable system, and its base area will determine the amount of foam that it is able to crush. Therefore, an approximate contact area for the crushable hemisphere can be approximated by the area of Biopan's base, which is 829.58-cm^2. This gives Biopan a conservative safety factor of 20 for required crushable area.

5. DESIGN & VISUALIZATION

The final design and configuration of BioDOME is shown in Figs. 17, 18 and 19. It is a $45°$ sphere-cone with semi-exposed aft-body. The rim of the vehicle is sized to 88-cm wide to provide enough drag area to achieve an allowable ballistic coefficient, while fitting inside the fairing of a Pegasus® launch vehicle. The Biopan payload unit sits within a hemisphere of crushable carbon-foam, attached to a metal thin-ring structure at half-height (see Figs. 17 and 19). The metal-ring attaches Biopan to the forward aeroshell unit through three sliding mechanically-actuated rails. The parachute, electronics and reentry roll-control RCS components are

all stowed in the space between the aeroshell and the Biopan/hemisphere housing, as seen in Fig. 19.
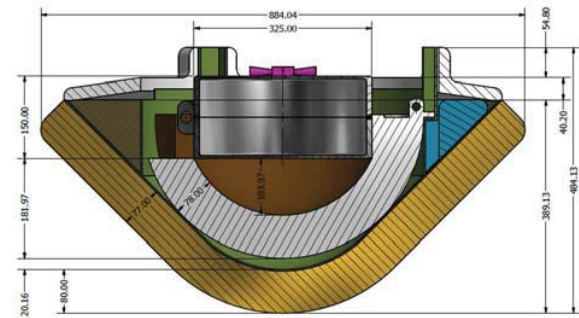

Fig. 17. Schematic View and Dimensions of the BioDOME Vehicle
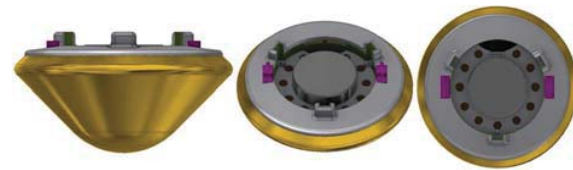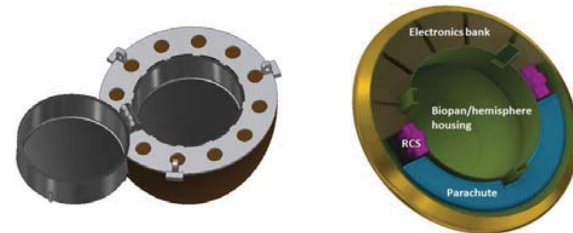

Fig. 18. General Views of the BioDOME Vehicle

Fig. 19. BioDOME Free-Flyer with Biopan Opened $180°$

On free-flyer missions, when the content of the Biopan has to be exposed to space, the pan with the metal-ring structures is lifted to the top of the vehicle on the rails, where the pan lids can be opened a full $180°$ without interference. On reentry, the Biopan is lowered and re-stowed. The design of sliding rails not only minimizes the vehicle's overall size and external geometrical complexities, it also lowers the center of gravity to improve the stability margin during the atmospheric flight phase. An aerodynamic aft-body with thin TPS is fitted only to the outer portion of BioDOME to protect the vehicle where recirculated hot gasses are expected to exist close to the vehicle wall [30].

On ISS-bound missions, although the entire BioDOME vehicle is too large to enter the station, the Biopan/hemisphere unit can be lifted from BioDOME's

sliding rails and the small diameter of the detached unit easily fits through ISS's cargo airlock. Potentially dangerous components such as the RCS and parachute mortar are also left outside the ISS in this operation.
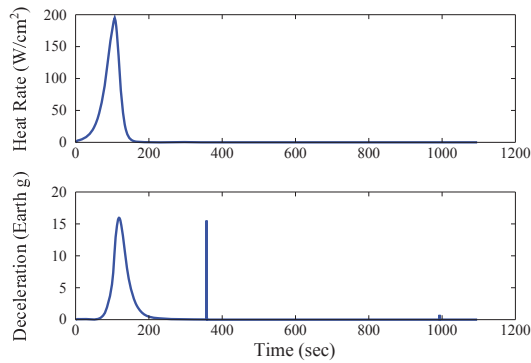

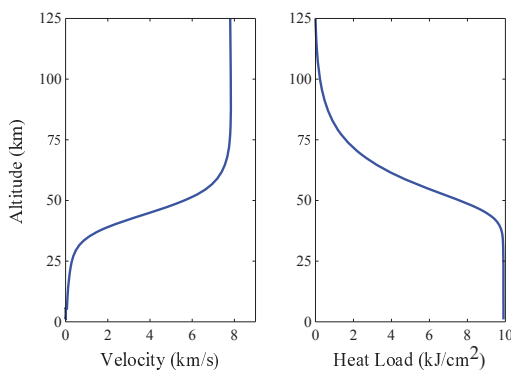Fig. 20. BioDOME Time Trajectory Profiles

Fig. 21. BioDOME Altitude Trajectory Profiles

On reentry, the vehicle encounters the peak heat rate and shortly after the peak deceleration, as demonstrated in Fig. 20. After the peak heating phase of hypersonic flight is over, the aft-body TPS is ejected to expose the parachute system. The BioDOME vehicle without parachute is expected to reach a subsonic terminal velocity. At $M = 0.20$, the parachute is deployed. A subsonic deployment allows the use of a single ringsail parachute to reduce BioDOME's mass. Although the parachute and its mortar are stowed within BioDOME's outer-rim, the chute's bridles are connected directly to anchors on the metal-ring that supports the Biopan. At 1000-m above the ground, BioDOME's aeroshell and subsystems are collectively jettisoned from the metal-ring. This reduces the weight of the remaining ring, crushable hemisphere, Biopan and parachute to 35.6-kg. A resultant touchdown velocity of 4-m/s or less limits the impact loading below 16g. The full trajectory profile

including the parachute deploy and the primary vehicle ejection is displayed in Figs. 20 and 21.

The crushable landing support of Biopan is shaped as a hemisphere to allow for non-vertical impacts during high winds conditions. The final mass breakdowns for BioDOME before and after ejection of the primary vehicle are displayed in Tables 3 and 4, respectively.

Table 3. BioDOME Mass Breakdown Before Primary Vehicle Ejection

System	Mass [kg]
Payload (Biopan)	15.0
Crushable Hemisphere	2.0
Parachute	13.2
RCS	12.0
Structures	15.0
TPS	15.0
Aftbody	2.0
Total Mass	**74.2**

Table 4. BioDOME Mass Breakdown After Primary Vehicle Ejection

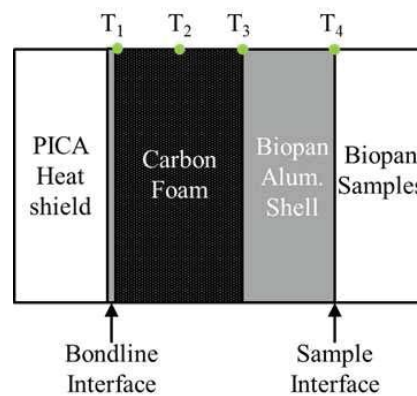| System	Mass [kg]
Payload (Biopan)	15.0
Crushable Hemisphere	2.0
Parachute	13.2
RCS	EJECTED
Structures	5.4
TPS	EJECTED
Aftbody	EJECTED
Total Mass	**35.6**

6. HEAT TRANSFER ANALYSIS

Fig. 22. Conceptual 1-D Thermal Analysis

A 1-D heat-transfer analysis was conducted to ensure that the interior temperatures of the Biopan did not exceed levels that are intolerable for its biological payload. The analysis assumed a worst-case location in the spacecraft where heat-shield's bulkhead is directly in contact with

the carbon-foam crushable landing system, while the carbon-foam is in contact with the aluminum Biopan. In the actual BioDOME design (see Fig. 17), direct contacts between the components are limited to two locations, and the majority of the Biopan will experience less direct heating. Fig. 22 below presents the one dimensional thermal analysis concept used to determine the temperature effect of entry heating on the Biopan samples.

A heat transfer analysis using a finite difference formulation predicted the temperatures at each of the four node locations in Fig. 22. The boundary condition applied at the T_1 location is the transient bondline temperature obtained previously. Thermal conduction, governed by Fourier's law, was enforced through the one dimensional stackup, between T_1 and T_4. From the thermal energy balance equation, energy storage was considered to obtain the transient thermal response through the stackup. Energy generation was neglected because no heat sources are present inside the material stackup. Carbon foam thermal properties were applied between T_1 and T_3 using the Duocel Reticulated Vitreous Carbon (RVC) Foam from ERG Aerospace Corporation [31]. Because Biopan has an aluminium shell surrounding the sample chamber, pure aluminium thermal properties were applied between T_3 and T_4. After completing the thermal finite difference analysis using the four nodes displayed in Fig. 22, temperatures T_2, T_3 and T_4 were obtained as functions of time. These temperature with time profiles are displayed below in Fig. 23.
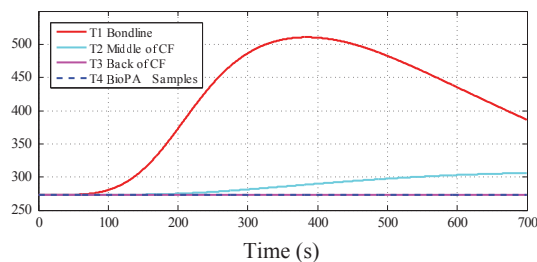

Fig. 23. Finite Difference Temperatures at Depth Using Four Nodes

Fig. 24 shows the time-progression across the carbon-foam material using a higher-fidelity heat transfer simulation with hundreds of spatial nodes. As shown, the heat flux from the bondline gradually penetrates the carbon-foam material to a depth of $\sim$60-mm. However, there was not a significant temperature rise propagated to the carbon-foam/Biopan sample interface at the heatshield jettison time of 700-s. Therefore, the heat-transfer analysis concluded that the biological payloads within Biopan will be safe against reentry heating.
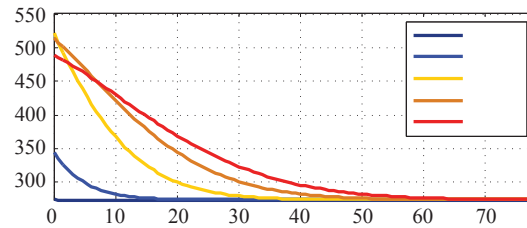

Fig. 24. Temperature vs Distance into Carbon-Foam

7. LAUNCH & REENTRY PROPULSIVE DEVICES

While this study focused mostly on the reentry vehicle concept, some considerations were given to launch vehicles, kick motors, and RCS thrusters for enabling spin stabilization. As mentioned previously, BioDOME shall be launched aboard a Pegasus® R launch vehicle. Pegasus® is able to deliver a payload directly into a $45\,^\circ$ inclination low-earth orbit launching over Wallops Flight Facility [16], as can be seen in Fig. 30 in the Appendix. This inclination also assures that ground track aligns with the Utah Test and Training Range (UTTR), as described later in Section 8. For these reasons, the free-flyer concept will target this orbit inclination, but any inclination $\geq 42\,^\circ$ is feasible for a UTTR landing.

A similar configuration would likely be used for the ISS option, assuming an approximately circular orbit at an altitude of 420-km and inclination angle of $51.6\,^\circ$. The identical Pegasus® launch vehicle scenario will be assumed to deliver the BioDOME vehicle and de-orbit kick motor to this orbit. However, an additional kick-motor may be necessary to perform an inclination change such that BioDOME can reach the ISS orbit.

The ISS return vehicle, which is identical to the free-flyer vehicle, shall be launched with a service module, battery, and a kick motor stage for performing the deorbit maneuver at the end of the mission. The ISS return vehicle mass was determined to be 74.6-kg, and an additional 15.4-kg will accommodate the combined mass of the service module and battery. After already reaching orbit, the kick motor will be required to provide ΔV of 923-m/s to deliver a total payload mass of approximately 90-kg to the specified entry altitude, velocity, and flight path angle. The rocket equation, shown below in Equation (12), was used to perform a discretized sizing of ATK kick motors.

$$\Delta V = g_0 I_{sp} \ln \frac{m_{initial}}{m_{final}} \qquad (12)$$

Fig. 25. Star 13A Kick Motor

The STAR 13A kick motor shown in Fig. 25, with a specific impulse of 286.6-s, is able to de-orbit and propel BioDOME to entry conditions with a total ΔV of 1007-m/s [32]. Since the ISS return vehicle likely requires more total ΔV than the free-flyer option, the same system can be used for both missions. Additionally, the STAR 13A kick motor has a diameter of 34.47-cm, a length of 63.78-cm, and a total mass of 47-kg [32]. The Pegasus® payload fairing constrains the payload vehicle to a maximum diameter of 97-cm, a maximum length of 213.6-cm, and a maximum mass of approximately 450-kg [16]. The BioDOME vehicle configured with the STAR 13A kick motor will fit comfortably within the payload fairing. The maximum acceleration experienced during launch is approximately 9.5-g's, which is well below BioDOME's maximum acceleration limit of 16 g's. This conceptual study focused on the reentry system, but the logistics for these additional systems would have to be considered during the preliminary design phase. Given the small size of BioDOME, it is expected that additional systems added during future design stages combined with the reentry vehicle will not exceed the mass and volume limitations of the launch vehicle's payload fairing.

After the de-orbit maneuver is completed, the kick-motor stage separates from the reentry vehicle. Given the passive ballistic trajectory chosen for BioDOME, it is desirable to ensure stabilization during reentry. One way to stabilize the reentry vehicle is through gyroscopic motion. The three most common options to rotate a spacecraft are reaction wheels, control moment gyros, and thruster systems. During regular mission operations, reaction wheels must be desaturated after they have run for an extended period, requiring additional thrust input or extra systems (i.e. magnetic torquers). This is not a necessary capability since the vehicle/payload will be recovered after landing. Thrusters are the only viable option to spin BioDOME for a short time right at the start of reentry. Reaction wheels and control moment gyros require a great deal of startup time to initiate spin and add unnecessary mass. In a thruster setup, only four 1-kg rockets would be required in addition to a 7-kg thrust chamber assembly. The amount of propellant needed to spin the vehicle 10 to 1000 rpm is still less than 1.5-kg overall using monomethyl hydrazine as the propellant.

The propellant mass is a small tradeoff when considering the benefits achieved with spin stabilization.

8. DISPERSION ANALYSIS & LANDING SITE

Monte Carlo simulation provides insight into the behavior of complex systems which are otherwise tedious to analyze. At the conceptual design level, this analysis may be implemented to catalogue influential metrics during entry, such as loading, heating environment, time to land, and downrange or crossrange. These parameters influence requirements, particularly on subsystem sizing, and additionally influence the potential landing ellipse. Numerical integration with a 6th order Cash-Karp adaptive timestep was employed for rapid trajectory analysis of 1000 individual simulated entries.

Table 5. Input Ranges and Distributions for Monte Carlo Analysis

Input Variable	Nominal	Variation	Distribution
Entry Vel. [m/s]	7800	± 25	Normal
Entry FPA [deg]	-5.0	± 0.080	Normal
Entry Alt. [km]	125	± 0.050	Normal
Ref. ρ [kg/m^3]	1.225	Earth GRAM	Uniform
Scale Height [m]	7200	0	Normal
Crosswind [m/s]	0	Earth GRAM	Normal

Table 5 provides the parameters of interest in the dispersion study, with focus on atmospheric entry conditions and the assumptions of the atmosphere. Given the entry from circular orbit, insertion velocity is assumed to be sub-circular, or less than 7.909-km/s. As previously discussed, the entry flight path angle was bounded by skip-out tendency and maximum loading environment for the lower and upper bounds, respectively. A similar dispersion analysis was performed for the Stardust mission at Earth utilized entry flight path angle variation of $\pm 0.08\,°$ to generate a normal distribution of entry angles [33]. The Stardust team noted that upon actual entry, flight path angle variation was expected to be no larger than $\pm 0.0017\,°$, with $\pm 0.10\,°$ variation implemented at the conceptual level to encapsulate all uncertainty upstream of entry. Thus, for this analysis, similar values are employed. For more realistic entry behavior, a $\pm 0.002\,°$ variation was used, while $\pm 0.08\,°$ was additionally used to provide a worst case behavior. Again, it is important to note that the $\pm 0.08\,°$ and $\pm 0.002\,°$ entry dispersion are for the conceptual phase only. With the added uncertainty of the deorbit phase kick motor, the entry angle dispersion will be iterated further to provide a more realistic value in simulation.

The atmosphere was modeled as exponential from a defined reference density at the surface, with a fixed scale height of 7200-m. A correction factor to capture

density uncertainty was additionally implemented, per the standards defined in the Earth Global Reference Atmospheric Model (Earth GRAM) [34]. While the raw reference data for Earth GRAM was not available, the general trends were published in the Startust EDL operations document, and were mimicked in this study. Fig. 26 provides the density to nominal density ratio as a function of altitude, where the dashed lines represent the 3σ boundary progression with altitude. Each of the five progressions of density ratio, shown in solid color, represents a unique atmosphere for the Monte Carlo simulation to propagate through, such that each run experienced a different atmosphere. These trends were developed by calculating the density ratio at any altitude as a normal distribution with a mean of the previous density ratio, and a variation related to the 3σ range at that altitude. Additionally, a 10% buffer was allowed for density ratio to fall outside of the 3σ boundary, as shown in the purple density ratio profile. Crosswinds were also modeled using the Stardust entry approximations, again taken from Earth GRAM, where the magnitude of wind decreases linearly towards 0-m/s at ground level from 35-m/s at 5.0-km.
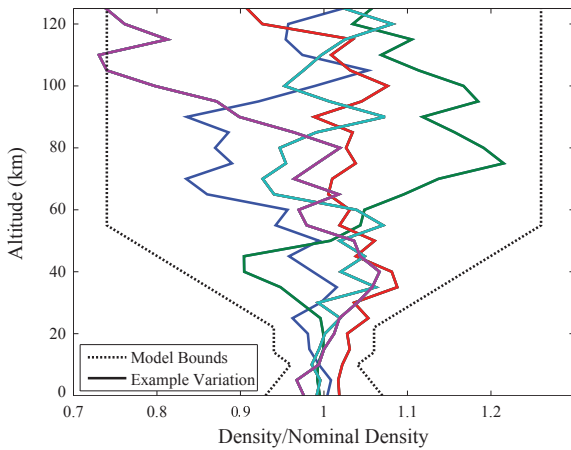

Fig. 26. Earth GRAM Implementation

To model parachute deployment, a 10 time-step quadratic delay was implemented at the parachute trigger condition to gradually increment $C_D A$ as the vehicle descended. With adaptive timestep integration, the duration of deployment varies with each dispersion case, but is typically less than 4-seconds. After the 10-step delay, parachute $C_D A$ is at a maximum. Cross track aggregation, arising from crosswind influence on the body, did not begin until the parachute was fully deployed. Parachute deployed at Mach 0.2, with the described deployment behavior. From the point of parachute deploy at Mach $0.2 + 10$ timesteps, the vehicle descended with a constant ballistic coefficient until an altitude of 400-m above the 1.0-km landing altitude. At

400-m, the Biopan system and the surrounding crushable hemisphere were ejected with the parachute. The resulting mass decrease from 74-kg to 35-kg resulted in touchdown velocities below 4.0-m/s - the critical landing velocity for the crushable system - as demonstrated in Fig. 27. Histograms of the resulting downrange distances from nominal for each uncertainty scenario are shown in Fig. 28. The resulting means, standard deviations, and ranges of various metrics from the simulations corresponding to $\pm0.08\,^\circ$ flight path angle variations are displayed in Table 6. The 3σ landing ellipse generated with 1000 simulations for the $\pm0.08\,^\circ$ entry dispersion case was 95.5-km $\times$ 1.36-km, and the equivalent 3σ landing ellipse for the $\pm0.002\,^\circ$ entry dispersion case was 45.5-km $\times$ 1.29-km. These ellipses are shown in Fig. 29.
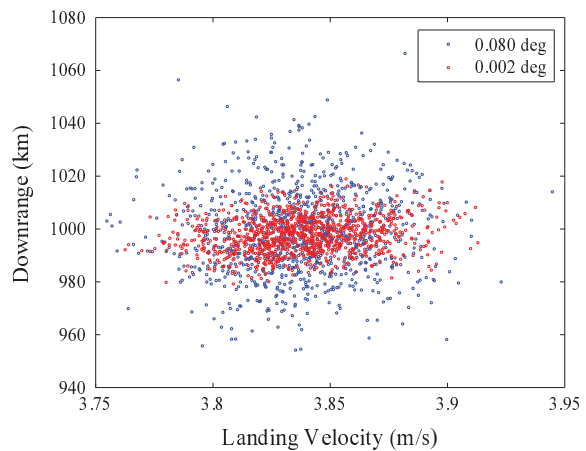

Fig. 27. Range and Landing Velocity Dispersion from Monte Carlo Analysis
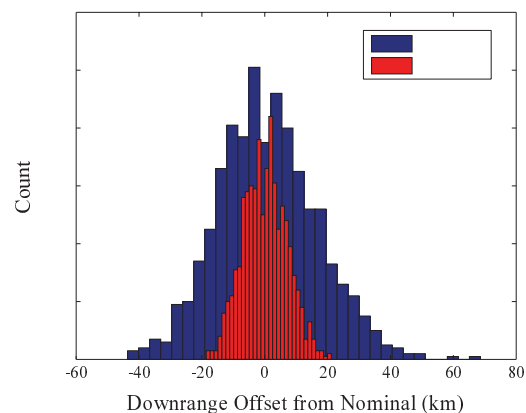

Fig. 28. Histogram of Downrange from Monte Carlo Simulations

Table 6. Output Ranges for Monte Carlo Analysis

Event	μ	σ	Range
Time to Land [s]	1092	21.35	1030 - 1157
Deceleration [Earth g]	16.09	0.545	15.4 - 18.4
Downrange [km]	998	15.9	954 - 1066
Heat Flux [kJ/cm^2]	195	5.02	179 - 211
Heat Load [kJ]	9.89	0.162	9.4 - 10.5
Crossrange [km]	4.35	0.22	3.64 - 5.17
Touchdown Velocity [m/s]	3.83	0.027	3.75 - 3.94

The Utah Test and Training Range (UTTR) was chosen as a landing site due to the requirements history established by the Genesis and Stardust missions, including the detailed hazard analysis that is required by NASA for any Earth reentry and landing missions [35]. This is also a potential landing site for future missions including the Earth Entry Vehicle (EEV) for the Mars Sample Return (MSR) project, which chose this site not only because of the reduced population hazards for this remote facility, but also because of the nominally soft terrain that can cushion the impact of its parachute-free design [28]. In fact, this silty desert floor greatly contained the debris scatter of the Genesis re-entry vehicle when it crashed hard into the ground after its parachute failed to deploy

[36]. Thus, this soft terrain may enable sample recovery for BioDOME even in the event of parachute system failure.

The bounds of UTTR are displayed in Fig. 29 with the Monte Carlo generated landing ellipses for an ISS return mission overlaid. The UTTR Green Fence represents conservative bounds for an acceptable target such that the landing is contained within the testing range, and several geographical landing hazards are displayed on the map as well. As can be seen, even the worst-case scenario ellipse generated from allowing entry flight-path angle between $\pm 0.08\,°$ is almost entirely contained within the Green Fence, avoiding most land hazards, the undesirable Yellow Divot, and the Dugout Keepout Zones where UTTR personnel may be stationed. The map includes topographical data for the region acquired from the Shuttle Radar Topographical Mission database, which shows that the elevation for most of the landing ellipse is just over 1.0-km altitude [37]. A quick analysis of Census block population in the region showed that very few people live along the proposed reentry ground track, with the only significant population density concentrated in Salt Lake City nearly 90-km northeast of UTTR [38].
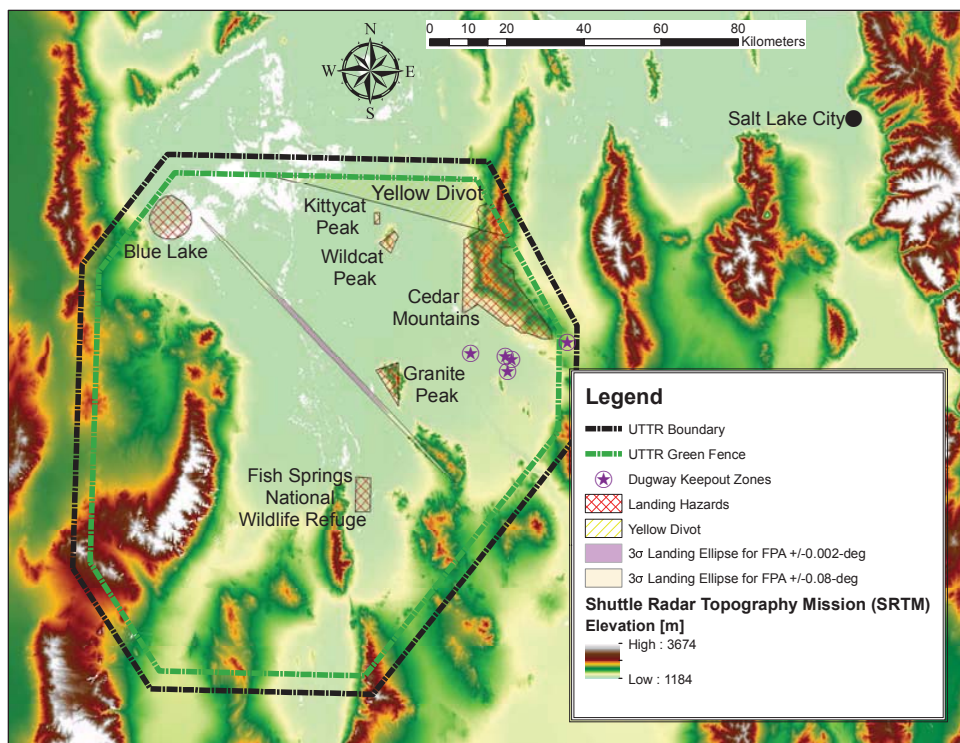

Fig. 29. Utah Test and Training Range (UTTR) with Landing Ellipses and Hazards

9. CONCLUSION

Preliminary sizing of the BioDome system for biological sample entry to Earth resulted in a ballistic, $45°$ sphere-cone, 0.88-meters in diameter. This system is capable of holding as many biological samples as the current Biopan architecture, and these samples may be exposed to space while in orbit and then sealed for reentry. In addition, the system limits maximum deceleration throughout flight to 16 g's via a shallow flight path angle of $5°$, an 8-m parachute deployment, and a crushable hemisphere system to cushion the impact g's of Biopan after primary vehicle separation. Under the parameters of dispersion analysis, crossrange and downrange were limited to $\pm$1.5-km and $\pm$30-km, respectively, while landing velocity was $\leq$4.0-m/s for all cases.

10. RECOMMENDATIONS FOR FUTURE STUDY

Given that the vehicle studies performed thus far are at a conceptual level, a second overall iteration with more refined subsystem analysis is the natural next step. With the down selection of candidate configurations complete, the first steps would be to develop refined vehicle sizing, and to support the implemented terminal descent timeline. A more precisely defined vehicle size and configuration will ultimately better define the loading and heating environment, which will update the thermal protection and parachute sizing. Further, the current parachute deployment method assumes the flight system will know the Mach environment and the altitude above ground level to first deploy the parachute and subsequently jettison the main structure. Two avenues may exist: (1) include hardware, such as radar or sonar, to actively seek for the ground; (2) develop a simple algorithm, dependent on timing from a particular event. The latter may be more reasonable as it is similar to the Pathfinder parachute algorithm, which implemented a time delay as a function of loading behavior. Additionally, a detailed structural analysis leveraging newer, light-weight materials could be explored to introduce significant savings in structural weight and reduce the ballistic coefficient of the vehicle.

11. REFERENCES

[1] Space REF, "ISS Spacecraft: Progress," http://www.spaceref.com/iss/spacecraft/progress.html, cited October 2014.

[2] Japanese Aerospace Exploration Agency (JAXA), "H-II Transfer Vehicle 'Kounotori' (HTV)," http://global.jaxa.jp/projects/rockets/htv/, cited October 2014.

[3] European Space Agency (ESA), "Automated Transfer Vehicle," http://www.esa.int/Our_Activities/Human_Spaceflight/ATV, cited October 2014.

[4] SpaceX, "Dragon," http://www.spacex.com/dragon, cited October 2014.

[5] Orbital Sciences Corporation, "Cygnus: Cargo Delivery Spacecraft for the International Space Station (ISS)," http://www.orbital.com/AdvancedSystems/Publications/Cygnus_factsheet.pdf, cited October 2014.

[6] Desai, P. N., Lyons, D. T., Tooley, J., and Kangas, J., "Entry, Descent, and Landing Operations Analysis for the Stardust Entry Capsule," *Journal of Spacecraft and Rockets*, Vol. 45, No. 6, November - December 2008, pp. 1262 – 1268.

[7] Terminal Velocity Aerospace LLC, "Delivering a Suite of ReEntry Devices (REDs) to Enhance Safety and Promote Space Utilization," http://www.tvaero.com/products.shtml, cited October 2014.

[8] Terminal Velocity Aerospace LLC, "Returning Unprecedented Reentry and Breakup Data to Serve the Needs of Safety and Design Communities Today," http://www.tvaero.com/red-data.shtml, cited October 2014.

[9] Intuitive Machines, "Science Sample Return Vehicle for International Space Station National Laboratory," http://intuitivemachines.com/news/trv/, cited October 2014.

[10] Noetzel, R. T. et al., "BIOPAN Experiment LICHENS on the Foton M2 Mission Pre-Flight Verification Tests of the Rhizocarpon Geographicum-Granite Ecosystem," *Advances in Space Research*, Vol. 40, 2007, pp. 1665 – 1671.

[11] Japan Aerospace Exploration Agency (JAXA)/ Mitsubishi Heavy Industries, Ltd., "Japanese Experiment Module (JEM)/Kibo (Hope)," http://www.nasa.gov/externalflash/ISSRG/pdfs/jem.pdf, cited November 2014.

[12] NASA Spaceflight, "International Space Station: EVA," http://spaceflight.nasa.gov/station/eva/outside.html, cited November 2014.

[13] Erasmus User Centre and Communication Office (HME-HE), *European Users Guide to Low Gravity Platforms*, European Space Agency (ESA), UIC-ESA-UM-0001, Issue 2, Revision 0 ed., 2005, "Chapter 6: FOTON Retrievable Capsules".

[14] Deguchi, S., Shimoshige, H., Tsudome, M., Mukai, S., Corkery, R., Ito, S., and Horikoshi, K., "Microbial Growth at Hyperaccelerations up to 403,627xg," *Proceedings of the National Academy of Sciences*, Vol. 108, April 2011, p. 7997.

[15] Demets, R., Schulte, W., and Baglioni, P., "The Past, Present, and Future of BIOPAN," *Advances in Space Research*, Vol. 36, July 2005, pp. 311–316.

[16] Orbital Sciences Corporation, *Pegasus® User's Guide*, Release 7.0 ed., April 2010.

[17] Lees, L., "Hypersonic Flow," *Fifth International Aeronautical Conference*, Institute of Aeronautical Sciences, New York, NY, 1955, pp. 241 – 276.

[18] Milos, F. and Chen, Y., "Comprehensive Model for Multicomponent Ablation Thermochemistry," *35th AIAA Aerospace Sciences Meeting and Exhibition*, No. AIAA 97-0141, NASA Ames Research Center, American Institute of Aeronautics and Astronautics, Inc., Reno, NV, January 1997.

[19] Kuhlman, T. L., "Thermo-Chemical-Structural Analysis of Carbon-Phenolic Composites with Pore Pressure and Pyrolysis Effects," Document HI-017F/1.2.5, Solid Propulsion Integrity Program (SPIP), August 1992.

[20] Sepka, S., Wray, A., Prabhu, D., Kornienko, R., and Radbourne, C., "Testing of SLA-561V in NASA-Ames Turbulent Flow Duct With Augmented Radiative Heating," *42nd AIAA Thermophysics Conference*, No. AIAA 2011-3619, ERC, Inc., NASA Ames Research Center, American Institute of Aeronautics and Astronautics, Inc., Honolulu, HI, June 2011.

[21] Ewing, E., Bixby, H., and Knacke, T., "Recovery System Design Guide," Tech. Rep. AFFDL-TR-78-151, Air Force Flight Dynamics Laboratory, 1978.

[22] "Materials: Fabric/Cloth," http://www.parachutefactory.com/03_mat/mat.php?cnum=41, 2011.

[23] Witkowski, A. and Bruno, R., "Mars Exploration Rover Parachute Decelerator System Program Overview," *17th AIAA Aerodynamic Decelerator Systems Technology Conference*, Pioneer Aerospace Organization and Jet Propulsion Laboratory (JPL), American Institute of Aeronautics and Astronautics, Inc., 2003.

[24] Pleasants, J. E., "Parachute Mortar Design," *Journal of Spacecraft and Rockets*, Vol. 11, No. 4, 1974, pp. 246–251.

[25] Space Recovery Systems, Inc., "Study of Pressure Packing Techniques for Parachutes," Tech. Rep. ASD-TR-61-426, United States Air Force (USAF), Wright-Patterson Air Force Base, Ohio, 1962.

[26] Braun, R., "Planetary Entry, Descent and Landing Shortcourse Notes," Georgia Institute of Technology, Atlanta, Georgia.

[27] Mitcheltree, R., Kellas, S., Dorsey, J., Desai, P., and Martin, C., "A Passive Earth-Entry Capsule for Mars Sample Return," *7th AIAA/ASME Joint Thermophysics and Heat Transfer Conference*, Albuquerque, New Mexico, June 1998.

[28] Mitcheltree, R., Braun, R., Hughes, S., and Simonsen, L., "Earth Entry Vehicle for Mars Sample Return," *51st International Astronautics Federation Congress*, NASA Langley Research Center, Rio de Janeiro, Brazil, October 2000.

[29] Kellas, S., "Design, Fabrication and Testing of a Crushable Energy Absorber for a Passive Earth Entry Vehicle," Contractor Report NASA/CR-2002-211425., NASA Technical Reports Server, Fairfax, Virginia, April 2002.

[30] Mehta, R., "Numerical Simulation of Supersonic Flow Past Reentry Capsules," *Shock Waves*, Vol. 15, No. 1, March 2006, pp. 31–41.

[31] ERG Aerospace Corporation, "Duocel® Reticulated Vitreous Carbon (RVC) Foam," http://www.ergaerospace.com/RVC-properties.htm, cited February 2015.

[32] ATK, *ATK Space Propulsion Products Catalog*, September 2012.

[33] Desai, P. N., Mitcheltree, R. A., and Cheatwood, F. M., "Entry Dispersion Analysis for the Stardust Comet Sample Return Capsule," *Journal of Spacecraft and Rockets*, Vol. 36, No. 3, May - June 1999.

[34] Justus, C., W.R. Jeffries, I., Yung, S., and Johnson, D., "The NASA/MSFC Global Reference Atmospheric Model1995 Version (GRAM-95)," Technical Memorandum NASA TM-4715, National Aeronautics and Astronautics Administration (NASA), August 1995.

[35] Tooley, J., Lyons, D., Desai, P., and Wawrzyniak, G., "Stardust Entry: Landing and Population Hazards in Mission Planning and Operations," *AIAA/AAS Astrodynamics Specialist Conference and Exhibit*, No. AIAA-2006-6412, 2006.

[36] SpaceFlight Now, "Photo gallery shows Genesis landing mishap," http://www.spaceflightnow.com/genesis/

gallery/03.html, posted September 2004, [Accessed November 2014].

[37] USGS (2004), "Shuttle Radar Topography Mission, 3 Arc Second scene," Filled finished 2.0, Global Land Cover Facility, University of Maryland, College Park, Maryland, February 2000.

[38] United States Census Bureau, "TIGER Products," https://www.census.gov/geo/maps-data/data/tiger.html, cited November 2014.